Programmable icosahedral shell system as molecular basis for virus trapping

Christian Sigl[1], Elena M. Willner[1], Wouter Engelen[1], Ken Sachenbacher[1], Anna Liedl[1], Fenna Kolbe[2,3], Florian Wilsch[2,3], S. Ali Aghvami[4], Ulrike Protzer[2,3], Michael F. Hagan[4], Seth Fraden[4], Hendrik Dietz[1]*

[1] Department of Physics, Technical University of Munich, Garching near Munich, Germany
[2] Institute of Virology, School of Medicine, Technical University of Munich, Munich, Germany
[3] Helmholtz Zentrum München and German Center for Infection Research (DZIF), Munich partner site, Munich, Germany
[4] Department of Physics, Brandeis University, Waltham, MA, United States

*Please address correspondence to: dietz@tum.de

Abstract

We describe a programmable icosahedral canvas that allows self-assembly of a wide family of virus-sized icosahedral shells. The canvas is formed from triangular building blocks constructed from DNA. The building blocks feature topographic lock-and-key interactions to specify distinct bonds on the icosahedral canvas. Various user-defined objects can be sculpted on the canvas, including half shells, full shells, and shells with user-defined openings. We experimentally created shells with molecular masses ranging from 43 to 925 Megadaltons (8 to 180 subunits) and with internal cavity diameters ranging up to 280 nm, and validated their structures using cryo electron microscopy. The objects form in simple one-step reactions with few defects and at high yields ranging from 95% to 40% and can be easily modified with other DNA structures, antibodies and small molecules. Our programmable icosahedral canvas system could provide a route to virus deactivation, premised on the concept of engulfing whole viruses in protective shells for blocking molecular interactions between virus and host cells. We engulfed hepatitis B virus core particles to demonstrate the feasibility of our virus-trapping and interaction-blocking concept. In addition to trapping viruses, potential applications of our programmable canvas include uses as stimuli-responsive macromolecular compartments that can be directly triggered by soluble antigens, which we also show experimentally.

Introduction

Viral infections cause enormous suffering and morbidity and impose huge drains on societies and economies in health care costs and lost work time. The burden of virus infections is likely to further increase due to habitat encroachment by humans, urbanization and megacities with increasing population density, increasing travel not only locally but also far distance, and numerous other drivers of disease emergence (*1*). Viruses are the pathogen class most likely to adapt to new environmental conditions because of their short generation time and genetic variability allowing rapid evolution (*2*). For the majority of viral

diseases, no effective treatment is available. Emerging virus threats require a rapid response, but broadly applicable ready-to-use antivirals do not exist.

Here, we use nanoengineering to establish the molecular basis for an unconventional antiviral concept: rather than targeting virus-specific proteins or enzymes by small molecules as current antivirals do, we propose to engulf whole viruses within *de novo* designed macromolecular shells to effectively block molecular interactions between virus and host cells (Fig. 1A). Our concept is specifically inspired by retroviral restriction factors of the mammalian immune defense that can inhibit invading viruses. In particular, the natural restriction factor TRIM5α assembles into a hexagonal shell surrounding entire HIV-1 retroviral capsids (*3, 4*). The TRIM5α example suggests that sterically occluding an entire virus by engulfing it in principle could be an effective therapeutic strategy.

Realizing target-specific virus engulfment synthetically poses fundamental nanoengineering challenges. It requires constructing well-defined massive molecular complexes on the scale of whole viruses, which may appear a daunting task. These complexes must furthermore either form dynamically around viruses or be able to swallow up entire viruses. To be of broad applicability, the shell system should be adaptable in order to cover the wide range of dimensions of viral pathogens (~ 20 nm to ~ 500 nm (*5*)). To be of any use as a potential antiviral, the shell material should be amenable to cost-efficient mass production, non-toxic and biodegradable. Furthermore, the shell material must be chemically addressable to modularly include virus-specificity conferring moieties on the shell interior, ideally in multivalent configurations that match the repetitive surfaces of viruses. Multivalency can ensure tight binding even for weak virus-binding molecules. Modularity enables using the same type of shell "platform" to target a variety of viruses. Since the shell material, rather than the moieties directly contacting the virus, will prevent access to the viral surface, *any* virus binder (e.g. non-neutralizing antibodies or aptamers) could then in principle be utilized.

The self-assembly of macromolecular complexes proceeds without external guidance or energy input. Hence, all information about the geometry of a desired target object must be encoded by the shape of its subunits and by the local interactions between them (*6*). Based on this principle, protein design and DNA nanotechnology may be employed to create biocompatible, mass-producible objects with user-defined shapes. Protein designers have previously succeeded in creating artificial macromolecular cages (*7-10*) by combining and modifying natural non-viral protein scaffolds that display suitable oligomerization symmetries. While *de novo* protein cages are an impressive feat of protein engineering, current artificially designed protein-cages are much smaller than the vast majority of natural viruses and cannot be easily modified. DNA nanotechnology (*11-16*) can create discrete objects with structurally well-defined 3D shapes (*17, 18*), including higher-order objects (*19-23*) with molecular masses exceeding one Gigadalton (*24*). However, these previous designs and the underlying concepts yield objects that are either too small, assemble with insufficient yields, do not match the shapes of viruses, or are too flexible or too skeletal to be suitable for effectively occluding a trapped virus.

Here, to meet the manifold requirements for target-specific virus engulfment, we designed and created a programmable icosahedral shell "canvas" by adapting symmetry principles known from natural viral capsids. The canvas can be scaled to match the size and

symmetry of the target pathogen. On this icosahedral canvas, designers can sculpt a variety of shapes, including full shells, pentagonal vertices, (spherical) half-shells, and shells with virus-sized openings using rational design decisions. Synthetic molecular constructs may be thus created that can either assemble around viruses to enclose them, or that can swallow up entire viruses, as we will show.

Results

Shell canvas design principles

Caspar and Klug elucidated the geometric principles that govern the structure of natural viral capsids in 1962 (*25*) by mapping a 2D triangulated net of protein positions to a 3D surface with positive curvature, through systematic replacement of 12 six-fold vertices with five-fold vertices. According to Caspar and Klug theory, which has been expanded recently (*26*), the number of distinct environments occupied by proteins within an icosahedral capsid is described by its triangulation number (T-number), which can be computed by a triangular net projection of the arrangement of pentamers and hexamers within an icosahedral capsid ($T=h^2+hk+k^2$, Fig. 1B). The total number of proteins required to build a natural capsid is T times sixty. This is because natural protein subunits are, by default, asymmetric and homo-trimerization is minimally required to construct a three-fold symmetric subunit that can assemble into an icosahedral shell with twenty triangular faces. To build larger capsids, viruses use more than one capsid protein or capsid proteins that can adopt different conformations. The structure of natural virus capsids and their abstract representation in the form of Caspar and Klug's triangular net projection (Fig. 1B) forms the basis for our synthetic programmable icosahedral shell canvasses, which we analogously classify using a T-number.

To practically implement the desired icosahedral canvas, we designed pseudo-symmetric triangular subunits (Fig. 1C) based on multi-layer DNA origami concepts. Every side of a triangular subunit is the equivalent of one protein subunit of a natural viral capsid. The overall canvas scale and type is controlled by geometric instructions provided by the triangular subunits. These instructions are given by the choice of the particular length of each triangular edge, by a unique topological pattern per edge for controlling pairwise edge-to-edge interactions within a set of different triangle units, and by a particular choice of the bevel angle of the edges, which controls the effective curvature of the shell. Since in our system each triangular edge represents one protein, the Caspar and Klug triangulation number now gives the number of unique triangular edges required to build a particular icosahedral canvas shell. Hence, T=1 and T=3 shells may both be built with a single triangle, with three identical edges for T=1 and three different edges for a T=3 shell (Fig. 1C, 1D, left). A T=4 shell canvas requires two separate triangular subunits, for example, one triangle with three unique edges and another with three identical edges (Fig. 1C, 1D, middle). A T=9 shell requires three different triangles, each having three unique edges (Fig. 1C, 1D, right). The greater the T number, the greater the overall number of triangles per target shell, given by 20T. We used design solutions in which all triangle bevel angles for a particular target shell were the same. While T=9 was the largest canvas we set out to build, we also designed triangular subunits for a smaller octahedral container ("O") (Fig. 1C, 1D, left).

Subunit and shell canvas assembly

We used iterative design with caDNAno (*27*) paired with elastic-network-guided molecular dynamics simulations (*28*) to produce candidate design solutions that fulfilled desired geometrical specifications. To approximate target bevel angles, we tuned the helical connectivity of the triangle edges in the vertices (fig. S1). These candidate designs were then encoded in DNA sequences using the methods of DNA origami. We produced the corresponding sets of oligonucleotides, and self-assembled the triangle variants in one-pot reaction mixtures (*29*). Gel-electrophoretic folding quality analysis demanded some design iterations to improve triangular subunit assembly yields (fig. S1). To validate the 3D structures of the designed triangles, we studied all triangle subunits using cryo transmission electron microscopy (cryo-EM) single particle analysis (Fig. 2). The resulting 3D electron maps had resolutions ranging from 13 to 22 Angstroms (figs S2-S9), which allowed us to evaluate the overall 3D shapes, the observed versus desired bevel angles (table S1, deviations within 5°), the correct positioning of all helices, the correct shape of the designed lateral protrusions and recesses for edge-to-edge docking, and the occurrence of systematic folding defects. For instance, one triangle variant (T_{hex1}) had a systematic structural defect at one of its vertices which decreased its ability to form lateral edge-to-edge interactions (fig. S10). Based on the cryo-EM data, we refined the design and eliminated the defect.

The thus improved triangle variants are designed to self-assemble into full icosahedral shells (= fully populated canvas), which we tested experimentally. The desired shells did indeed self-assemble successfully (see methods) and had the expected dimensions, as confirmed by direct imaging with cryo-EM (Fig. 2A, see figs S11-S15 for additional images). Inspection of individual particles (Fig. 2A) and of 2D class averages (Fig. 2B-F) revealed particles displaying the designed symmetries. For example, the three symmetry axes of the octahedron (4-fold, 3-fold, 2-fold, Fig. 2B) and T=1 shell (5-fold, 3-fold, 2-fold, Fig. 2C) can be clearly seen. The particles of the higher-T-number shells had a more circular appearance due to the higher number of triangles per particles, and the underlying triangular net predicted from the Caspar-and-Klug representation became clearly visible (Fig. 2D-F). Since the individual particles displayed the designed symmetry, we determined 3D EM maps of the shells by imposing the respective symmetry (Fig. 2B-E). The resulting maps had resolutions ranging from 20 to 40 Angstrom. The resolutions of the octahedron and T=1 shell maps were sufficient to discern individual DNA double helices.

For the T=1 shell variant we determined a 3D map from the data without imposing any *a priori* symmetry, and this map was fully icosahedral and superimposed well with the sibling that we reconstructed with imposed symmetry, albeit at less resolution. This work successfully proved the concept of icosahedral symmetry (fig. S12E). We also successfully determined octahedron cryo EM maps with and without imposed symmetry (fig. S11E). We classified and treated cryo EM maps of shells that lacked one or multiple triangles separately from complete shells (figs S11D, S12D), allowing for quantitative assessment of target quality and yield. The cryo EM maps of shells with defects also displayed the designed overall symmetry. We examined the largest T=9 shells with negative stain EM tomography (Fig. 2F, fig. S16C). Sections through tomograms of assembled T=9 shells show fully closed shells as well as the correct arrangement of pentamers according to the designed T-number (arrows in Fig. 2F and fig. S16C).

To elucidate effects of orientational specificity of subunit-subunit interactions, we varied the bevel angle of the T=1 subunits from the ideal geometry (α=20.9°). We designed two additional variants of the T=1 triangle whose bevel angles deviated by +5° or -5° from the icosahedral ideal. The decrease or increase of the bevel angle caused the appearance of larger shell-like structures in addition to T=1 shells or octahedra, respectively (fig. S17). Based on these data we conclude that the correct target bevel angle in a T=1 triangle subunit must be matched within a range of +-5°.

Sculpting on the icosahedral canvas

Once the user has decided on a particular type of icosahedral canvas, the assembly of the triangular subunits forming said canvas can be programmed to cover only user-defined areas on this canvas. This option arises because the triangular subunits are designed to self-assemble into higher-order objects through lateral edge-to-edge interactions that only engage upon precise fit of shape-complementary topographic features on the triangle edges, whereas wrong binding partners are sterically rejected. It is the geometry of these features that specifies the edge binding partner, in analogy to lock-and-key interactions in proteins. To create the full shells, i.e. a fully populated canvas, only the minimum number of different topographic interaction patterns ("symmetries") is implemented as discussed above. Introducing additional types of topographic edge-to-edge interactions per triangular subunit allows reducing the symmetry in which the subunit may be integrated in the canvas. Furthermore, the stacking interactions can be modularly activated and de-activated, for example by shortening a strand terminus involved in a stacking contact or by adding unpaired thymidine terminal strand extensions, which will leave a particular triangular edge unpaired. Together, these features enable sculpting a variety of objects based on the icosahedral canvas in a programmable fashion.

To design such objects, we used the triangular net projection of the chosen icosahedral canvas type as a drawing board (Fig. 3 A-E). For example, in order to prepare half instead of full octahedra, complementary lock-and-key interactions of two edges of the triangular subunit are needed and one edge interaction must be deactivated (Fig. 3A). A pentagonal dome can be analogously created based on the T=1 icosahedral canvas (Fig. 3B). Building an icosahedral half shell requires two different triangular subunits, one that forms the pentagonal dome, and another that specifically docks onto the edges of the pentamer (Fig. 3C). A ring-like "sheath" may also be built by two triangles (Fig. 3D). To build a T=1 shell variant with one missing pentagon vertex, three triangular subunit variants with a specific interaction pattern are needed (Fig. 3E). We practically implemented the above discussed design variants using appropriately modified triangular building blocks (Fig. 3F-H, fig. S18). The building blocks self-assembled successfully into the desired higher-order objects based on their icosahedral canvas, which we validated experimentally by determining cryo EM solution structures (Fig. 3I-K, figs S19-S21). The resulting 2D class-averages and the 3D electron density maps revealed the structural features that we expected by their design.

Virus trapping

As outlined initially, we envision multiple strategies for using our programmable icosahedral canvas system to block viral surfaces from potential virus-cell interactions. One strategy consists in trapping virus particles in pre-assembled icosahedral shell objects (Fig. 4A,B).

Another strategy is assembling protective shells directly on the surface of viruses (Fig. 4C). We successfully realized all strategies. To demonstrate the virus trapping capability, we used hepatitis B virus core particles (HBV) as a safe, non-infectious model virus (Fig. 4A, red). To confer specificity, we conjugated anti-HBc 17H7 (Isotype IgG-2b) to the DNA shells by hybridization of ssDNA-labeled antibodies to a set of anchor points on the triangle subunits, which we predicted would render the interior of the shells sticky specifically for the target virus (Fig. 4A, cyan layer). Indeed, when we incubated HBV core particles with the thus-prepared DNA shells in approximately 1:1 stoichiometry, all free virus particles were effectively taken up by our shell particles, as seen by negative-staining TEM imaging (Fig. 4B, see also fig. S22). We did not observe any HBV binding in the absence of HBV antibodies conjugated to the shell interior (fig. S23A), nor in the presence of antibodies specific for other targets (fig. S23B). Similarly, when we incubated HBV core particles with antibody-labeled monomeric triangle subunits designed to form a T=1 shell, we observed that these triangles assembled a in thick shell around the HBV (Fig. 4C).

We performed cryo electron microscopy to convince ourselves of the proper capture of the target virus in our shells and determined 3D cryo EM maps of octahedral and T=1 half shells with trapped HBV core particles (Fig. 4D, E, see figs. S24-S25). These maps clearly show the feasibility of our virus-trapping system. For the half-octahedral variant, the majority of particles consisted of two opposing half octahedra coordinating a single HBV core particle in their middle (Fig. 4D). We observe the two half-octahedral shells in a variety of relative conformations on the shared HBV core particle (fig. S24). The micrographs and the cryo EM map also reveal signatures reflecting the antibodies that link the DNA shell to the trapped HBV core particle (Fig. 4D, right). Similar antibody signatures may be found in the image data with the half T=1 shell-HBV complex (Fig. 4E, right). Finally, we also trapped HBV core particles trapped in the much larger T=1 shells missing a pentagon vertex (see Fig. 4F). Because these “virus-traps” are much larger than the HBV particles, they can swallow up multiple HBV particles in their interior cavities (Fig. 4F, see fig. S22E,F).

Finally, to test the capacity of our shells to prevent a trapped virus to undergo interactions with cell surfaces, we performed *in vitro* virus blocking assays with HBV-binding antibodies immobilized on a solid phase mimicking a cell surface (Fig. 4G, fig. S26). We quantified the extent of HBV core particle binding to the solid phase via binding of an orthogonal HBV core-specific reporter antibody coupled to horseradish peroxidase (HRP). As in conventional enzyme-linked immunosorbent assays, residual HBV core particles that are bound to the surface and that are accessible for binding will be detected via HRP catalyzed production of a colorimetric signal. In the presence of our virus-engulfing shells (half T=1 shells), virus interactions with the solid phase were blocked up to 99% (Fig. 4G bottom), thus confirming the desired interaction-inhibiting capacity of our shells. Control experiments with shells lacking HBV trapping antibody resulted in minimal virus blocking compared to the signal generated by naked HBV core particles that represent baseline 0% virus blocking. HBV core particles directly incubated with the trapping antibodies but lacking any shells also showed minimal virus blocking. This result directly demonstrates the beneficial effect of multivalent binding of the antibodies in the context of the surrounding shell: the soluble antibodies by themselves do not achieve a passivating function even though they are added at 400-fold excess over HBV particles. Importantly, with as few as five trapping antibodies per protective shell we achieved a virus blocking efficiency of greater than 80%. These findings

demonstrate that our shells, and not the antibodies used for holding the virus inside the shell, shield the virus from its exterior by steric occlusion. Therefore, our virus-trapping shells indeed accomplish the desired protective function.

Antibody-stabilized shells enable antigen-triggered disassembly

Our shell canvas concept can also be generalized beyond using base pair(stacking) interactions for shell stabilization, which enables implementing a molecular logic to control the state of the shells. To show this possibility, we prepared a shell design variant in which we displayed multiple steroid molecules (digoxigenin) per edge of the triangular subunits (Fig. 5A). The steroids are placed such that in the context of the shell their pairwise distance across the direct boundary between two neighboring triangular subunits is around 12 nm. This distance matches approximately the distance between the two antigen-binding epitopes of a divalent IgG antibody, and we thus expect that the IgG can bind across triangular subunits to serve as a molecular staple. To test this concept, we self-assembled the shells at high ionic strength conditions where the base pair stacking is active, added Anti-Digoxigenin IgG antibodies to the solution, and then removed cations from solution. Under these conditions the triangular edge-to-edge subunit interactions are no longer conferred by base pair stacking contacts, but instead rely solely on the binding of the divalent antibody “staples”. Addition of a soluble antigen then induces shell disassembly by competitive reactions which remove the antibodies from the shell surface, as seen by a vanishing band indicating complete shells and emergence of a band indicating triangular monomers in gel electrophoretic mobility analysis (Fig. 5B). The antigen-triggered disassembly occurs at a particular antigen threshold concentration (here: EC_{50} = 1 μM, Fig. 5C). The threshold depended on design details such as number of antibody crosslinking sites and can presumably be further tuned. We also determined a cryo-EM structure of antibody-stapled icosahedral T=1 shell (Fig. 5D, fig. S27), which clearly revealed the IgG antibodies on the shell surface, with the Fc fragments pointing away from the shell.

Toward macromolecule-proof shells

Our current shell variants add a ~15 nm thick DNA layer around a trapped virus particle (not counting the internal spacing created by the layer of virus-binders), and it is hard to imagine how cell-virus interactions could still take place through such thick envelopes. However, our current designs do feature several apertures, notably the cavities in the triangular subunits, which may permit residual interactions. As a demonstration for a route toward sealing the cavities in the triangular subunits we built a DNA brick having a triangular cross-section roughly corresponding to the dimensions of the triangular cavity in the shell subunits. We anchored the brick via multiple attachment points to the outer surface of a T=1 shell triangle (fig. S28 for design details, see fig. S29 for a cryo-EM solution structure of the brick) and partially plugged it into the cavities in the shell subunits. The brick may also act as a spacer that further separates cell surfaces from those of viruses trapped in shells by another 40 nm. The brick can be added to already assembled shells or, alternatively, the triangles and brick units can also first be dimerized, followed by triggering shell assembly. Both routes yield fully assembled “spiky” T=1 shells under the same conditions as for the unmodified T=1 shell. We solved a structure of the spiky T=1 shell using cryo-EM single particle analysis (Fig. 5E, fig. S30). The resulting map readily overlaps with those of the unmodified T=1 shell, but the central opening of the triangle shell subunits is now blocked by the added channel

module (fig. S30E). The fact that the cavity-plugging with the DNA brick readily worked demonstrates the robustness and structural modularity of our shells. The brick may also be considered as a mimic for previously described DNA-based membrane channels (*30*) or for any other functional module that one wishes to attach to a shell. As a demonstration for how to load a molecular cargo, we prepared shell variants in which a single 8064 bases-long DNA single strand is packaged. We also added gold nanoparticles to the cargo to exemplify the possibility to load the shells with inorganic material. Single-particle TEM tomograms validate the successful encapsulation (fig. S31).

Shell yield and stability

Having established the principles of our programmable icosahedral canvas, the feasibility of virus trapping, and logic control over the state of the shells, we evaluated practical aspects such as assembly yield and stability in physiological conditions where the system is ultimately expected to be applied. Low-density gel electrophoretic mobility analysis (Fig. 6A, fig. S32) revealed that shell assembly proceeded by disappearance of the triangular monomers, appearance of a smear indicating the presence of oligomeric species, followed by emergence of a dominant high intensity band, which in all cases corresponded to the fully formed shell. Octahedra and T=1 shells formed within 15 and 60 minutes, respectively, which is sufficiently fast to enable self-assembly of these shells directly during the one-pot triangle-folding reaction (fig. S33). Octahedra formed with a final complete shell yield of ~95%. The T=1 shells formed with up to 70% yield. The T=3 and T=4 shells formed with about 40% yield (Fig. 6A). Subunit-exchange experiments with fluorescently labeled subunits revealed that under shell-favoring conditions triangles that are incorporated in closed shells do not exchange with solution (Fig. 6B, fig. S34A,B). Under equilibrium conditions (Fig. 4B, fig. S34C), triangles do exchange. For the intended application, shells should be stable without subunit turnover in physiological fluids, which we successfully realized through simple post-assembly processing steps. Specifically, we first assembled the shells under high ionic strength conditions and then applied UV point welding (*31*) to create additional internal covalent bonds in the triangle subunits. These photochemically created bonds can also be introduced across the stacking contacts at triangle edges (*31*). We then coated the shells with a mixture of oligolysine and PEG oligolysine (*32*). This two-step treatment allowed us to successfully transfer the shells into mouse serum, where the shells remained intact for up to 24h (Fig. 6C).

Discussion

We have experimentally demonstrated a symmetry-based approach for self-assembly of a series of programmable icosahedral shell canvasses with high yield and fidelity. Overall, with molecular masses ranging from 43 to 925 Megadaltons (8 to 180 triangle subunits, depending on the design), our shell assemblies were not only substantially larger than any other previously reported one-pot-assembled artificial macromolecular assemblies with defined size, but our shells also formed with orders-of-magnitude improved yields compared to previously built nucleic acid based polyhedra (*19, 24*).

In addition, we introduce a new stabilization concept that relies on antibody “staples” that span subunit interfaces, consequently allowing triggered disassembly by competition with soluble antigens. This concept could be further explored by installing specific combinations

of antibodies, thereby creating sophisticated molecular logic operations or tailoring dose-response curves. Since all stabilizing elements are integrated on the nanoparticle, our logic-gating mechanism is insensitive to dilution, which is a crucial requirement for potential future biomedical applications. The antibody-stapled icosahedral shells also realize a new type of protein-DNA hybrid structure (*33*), where the DNA components act as a geometrical scaffold and the protein component contributes stabilizing physical bonds.

The high programmability of the shell canvas allows sculpting various objects such as half-shells or shells with entry portals, which we propose as virus-neutralizing agents for trapping and inactivating viruses. We envision that trapping viruses in shells can decrease the viral load in acute viral infections and may help eradicating viral particles from the body or ex vivo from body fluids. Since the shells do not target any enzymes of the host metabolism as many current antivirals do, we expect them to be largely non-toxic even at the high doses required at later stages of infection, which could be a major advantage over many existing antiviral drugs. We tested the virus trapping successfully with HBV core particles as a model virus particle and achieved near complete inactivation by engulfing HBV in a surrounding shell. To realize the virus trapping, we mounted antibodies on the shell interior. However, other types of virus binders are readily conceivable. For example, host receptor domains or peptides known to be targeted by a viral pathogen (e.g. ACE-2 by CoV-2 (*34*)) and DNA / RNA aptamers could be used. In our design solution, a half T=1 shell featured sites for 90 virus-binding moieties facing the interior cavity. While it would be possible to create even more attachment sites, 90 is already a very high number. This high level of multivalency will be particularly useful for trapping pathogens for which only low-affinity binders are available. Furthermore, some of these sites could also be used to mount additional virus-binding moieties to enhance specificity, or for attaching molecules with proteolytic activity such as trypsin or proteinase K, which could endow the shells with virucidal activity by degrading surface proteins of trapped viruses.

Our icosahedral shells consist of DNA, which is durable, available commercially, and easily functionalized and modified, which we also used to our advantage in this work. Using DNA-based agents can potentially circumvent neutralization, phagocytosis and degradation by pathways of the innate and adaptive immune system targeting protein structures. However, although we could show successful stabilization of our shells in serum, at this point we cannot exclude that nucleic-acid specific reactions, i.e. activation of pattern-recognition receptors recognizing DNA (*35, 36*) or induction of DNA-binding antibodies may occur once the shells are applied *in vivo.* Testing our concept for trapping viral pathogens on a variety of viruses and assessing the neutralization capacity, as well as assessing potentially adverse effects *in-vivo*, are important challenges for the future. Here, we accomplished the important step of establishing the molecular basis for trapping viral pathogens.

Beyond the proposed application as virus-neutralizing agents, our programmable icosahedral canvas system also offers opportunities to create antigen-carriers for vaccination, DNA or RNA carriers for gene therapy or gene modification, drug delivery vehicles and protective storage containers. Our shell system may offer particular opportunities as alternative gene delivery vectors that can accommodate genomic information much larger as those that can be delivered currently with e.g. adeno associated viruses (AAV) (*37, 38*), which are popular gene therapy vectors. The nucleic acids to be

delivered could then also be combined with proteins or protein complexes rendering e.g. CRISPR/Cas based gene silencing or gene modification approaches safer and more efficient.

Acknowledgements

We thank B. Kick for help with the antibody-DNA conjugation and for scaffold preparation. This work was supported by a European Research Council Consolidator Grant to H.D. (GA no. 724261), the Deutsche Forschungsgemeinschaft through grants provided within the Gottfried-Wilhelm-Leibniz Program and the SFB863 TPA9 (to H.D.), the TRR179 (TP14 to U.P.), the German Ministry for Education and Research (BMBF) through StabVacB and DZIF project 05.806/907 (U.P.), the Netherlands Organization for Scientific Research (NWO, Rubicon program, project no. 019.182EN.037 to W.E.), the USA National Science Foundation through the Brandeis University Materials Research Science and Engineering Center DMR-1420382 (S.F. and M.F.H), and Award Number R01GM108021 from the National Institute Of General Medical Sciences (M.F.H).

Author contributions

H.D. designed the research. S.F. co-designed closed-shell self-assembly studies (Figs. 1, 2). C.S. performed shell subunit design, shell assembly and all structural studies (Figs. 1-6). E.W. performed shell modification and stabilization, and virus-binding inhibition experiments (Figs. 4-6), supported by A.L.. W.E. performed subunit exchange, antibody-based shell stabilization and antigen-triggerable disassembly experiments and virus-binding inhibition experiments (Figs. 4-6). K.S. performed auxiliary shell subunit geometry alteration experiments (fig. S17). F.K., F.W., U.P. contributed HBV samples, and generated and provided HBcAg antibodies. S.A. performed cargo encapsulation (fig. S31). M.H. contributed to shell design choices.

Figures and Captions

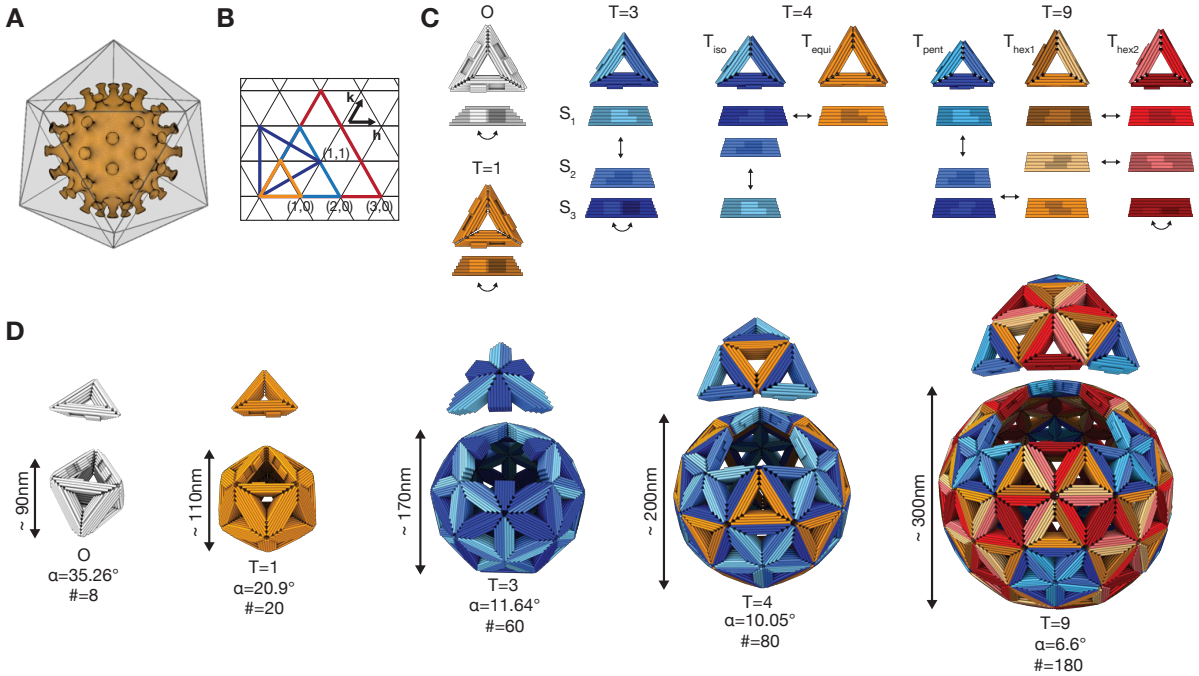

Fig. 1 | Design principles. (**A**) Icosahedral shell encapsulating a virus capsid. (**B**) Triangular net representation of icosahedral shells. Each colored triangle represents one of the 20 faces forming an icosahedron. The small triangles represent the triangular building blocks. (h,k) indicates the location of pentamers within a shell. (**C**) Cylindrical model of DNA-origami triangles assembling into the shells shown in (D). The edges of the triangles are beveled and modified with shape-complementary protrusions (light) and recesses (dark). The arrows indicate shape-complementary combinations. For design details see figs. S35 to S38. (**D**) Icosahedral shells formed by the triangles shown in (C). For each shell design, one of its 20 icosahedral faces has been displaced (see (B)) to help recognize the icosahedral symmetry. α is the bevel angle of the sides, # the number of DNA-origami triangles building the shell.

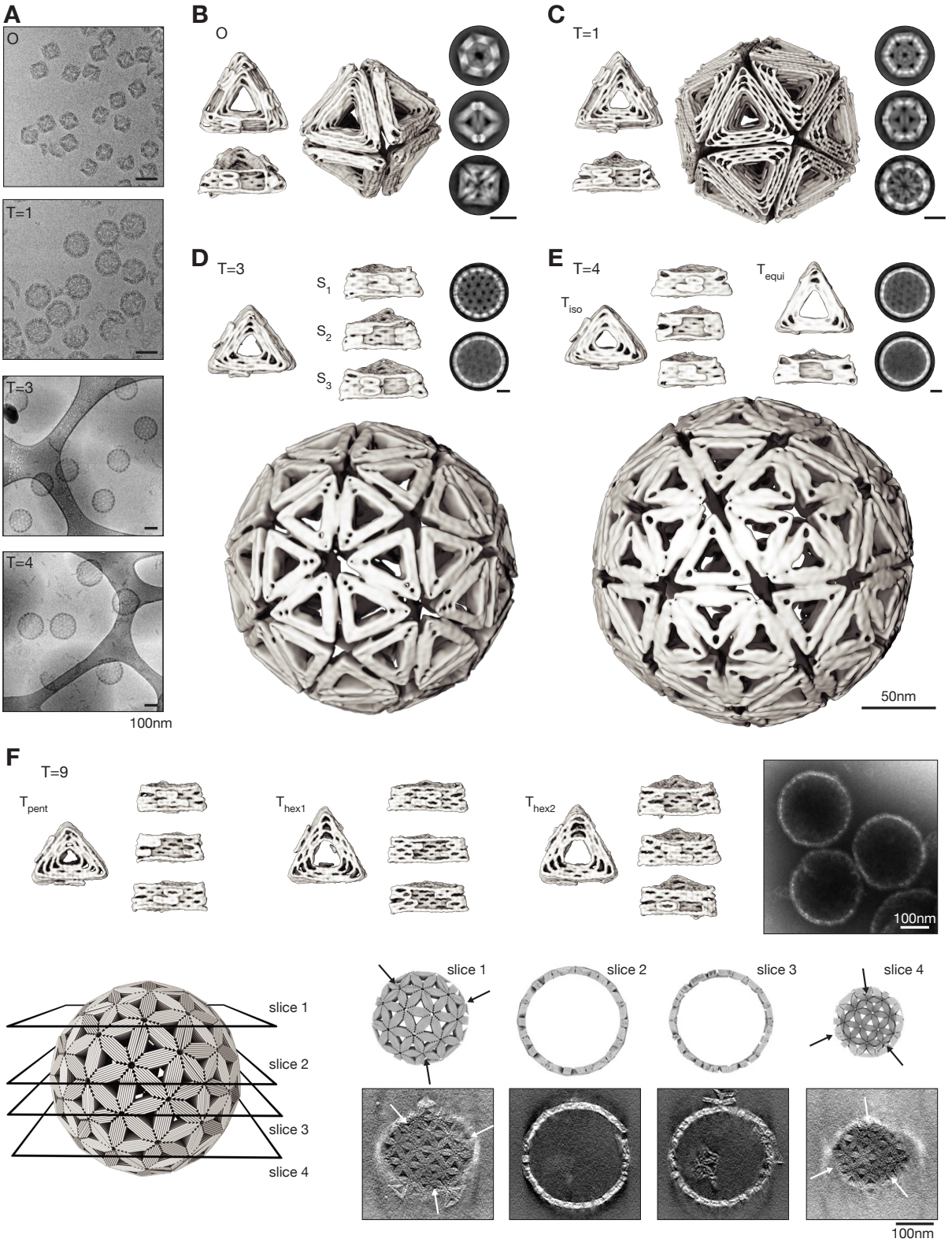

Fig. 2 | Structures of shells and of shell subunits. (**A**) Cryo-EM micrographs of assembled shells in free-standing ice (O, T=1) and on lacey carbon grids with carbon support (T=3, T=4). (**B** to **E**) Cryo-EM reconstructions of shell subunits and fully assembled shells (octahedron to T=4 shells). The two-dimensional class averages show assembled shells from different orientations. (**F**) EM validation of the T=9 shell design. Top left, cryo-EM reconstructions of the three triangles assembling into a T=9 shell. Top right, negatively stained EM micrograph of assembled shells. Bottom, comparison of slices through a model shell to slices of a tomogram calculated from an EM tilt series. The arrows indicate the positions of pentamers within the shell. See also Supplementary movies 1-5.

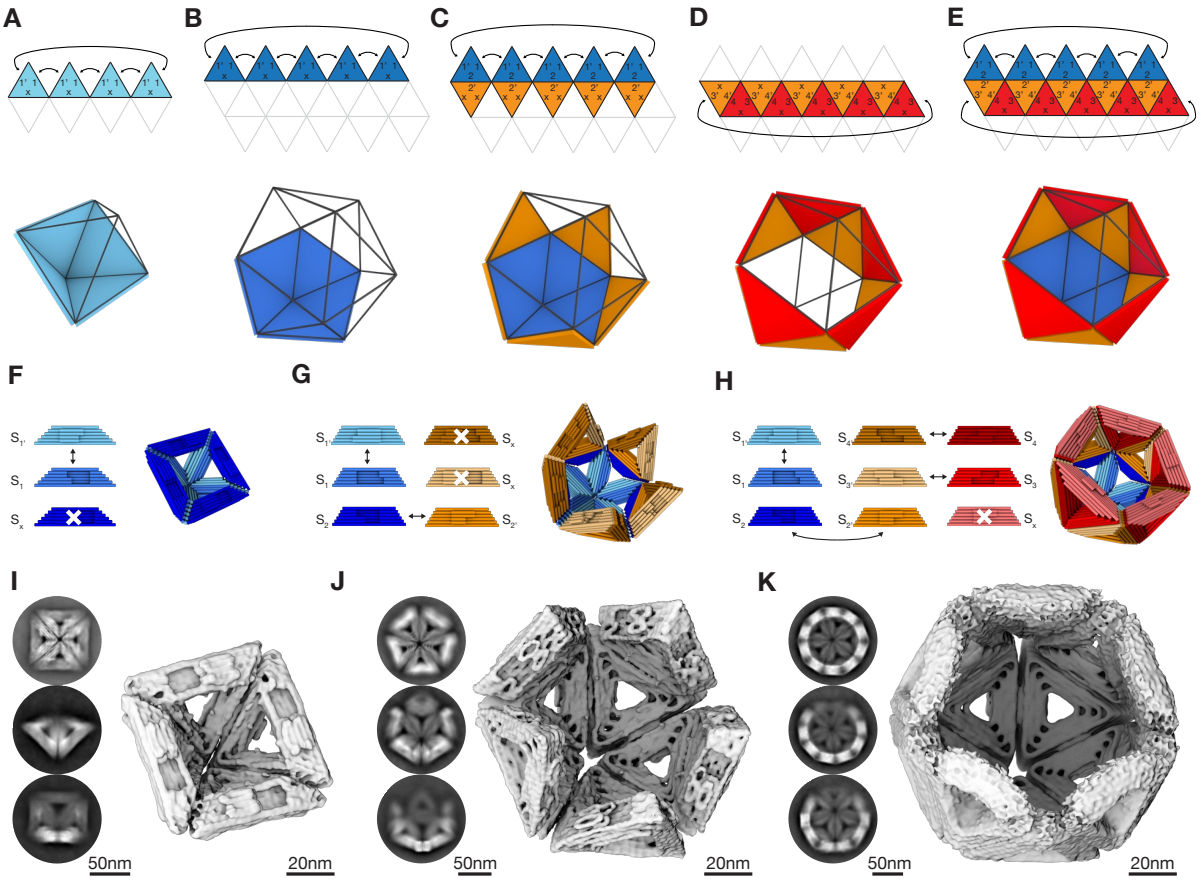

Fig. 3 | Sculpting on an icosahedral canvas. (**A-E**) Triangular net projection and schematics of different partial shells: half octahedral shell (A), pentamer (B), half T=1 shell (C), ring (D) and T=1 shells lacking a pentagon vertex (E). (**F-H**) Cylindrical models of DNA-origami triangles and corresponding partial shells of the half-octahedral shell (F), half T=1 shell (G) and T=1 shells lacking a pentagon vertex (H). The sides of the triangles are modified with protrusions and recesses. The arrows indicate shape-complementary sides. White crosses indicate deactivated interaction sites. For design details see figs. S39, S40. (**I-K**) Cryo-EM 3D reconstructions of the partial shells shown in (F-H). Insets give typical two-dimensional class averages showing assembled shells from different orientations.

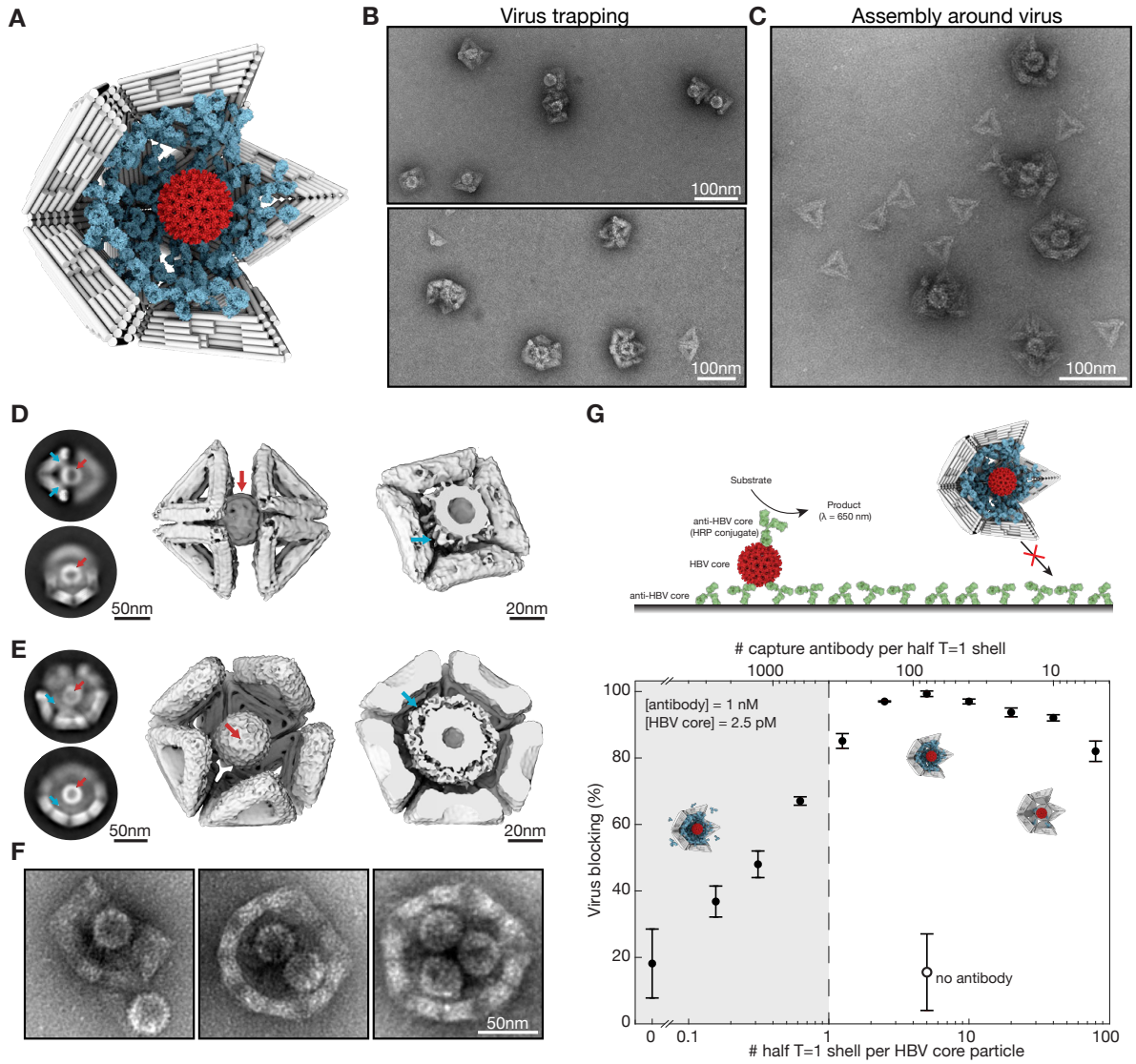

Fig. 4 | Trapping of hepatitis B virus (HBV) core particles. (**A**) Schematic representation of a half T=1 shell (white) equipped with antibodies (cyan) with a trapped HBV core particle (red). (**B**) Negative stain TEM images of HBV core particles trapped in half octahedral (top) and half T=1 (bottom) shells. (**C**) Negative stain TEM image of T=1 triangles modified with nine antibodies self-assembled around HBV core particles as templates. (**D**) Left: Two-dimensional EM class averages. Middle: Cryo-EM reconstruction of two octahedral half-shells coordinating a trapped hepatitis-B virus particle. See also Supplementary movies 6,7. Right: Cut through the octahedral-DNA shell cryo EM map with the HBV core particle trapped. The density around the HBV core particle stems from the antibodies connecting the HBV core particles to the octahedral shell. Red arrows: HBV core particle. Cyan arrows: antibodies connecting the shell to the HBV core particle. (**E**) Same as in (D) for the half T=1 shell. The electron density thresholds differ, which makes the HBV core particle look thicker in the T=1 half shell compared to the half octahedron (right). (**F**) Negative stain TEM images of T=1 shell with a missing pentagon vertex engulfing up to three HBV core particles. (**G**) *In vitro* virus blocking ELISA experiments. Top: Schematic representation of the ELISA experiment. Bottom: Filled dots indicate 2.5 pM HBV core particle incubated with pre-assembled mixtures of 1 nM oligonucleotide-conjugated capture antibody and various concentrations of half T=1 shells. The open dot represents a mixture of HBV core particles with T=1 half shells without any antibodies conjugated to it. Errors bars are standard deviation of triplicate measurements.

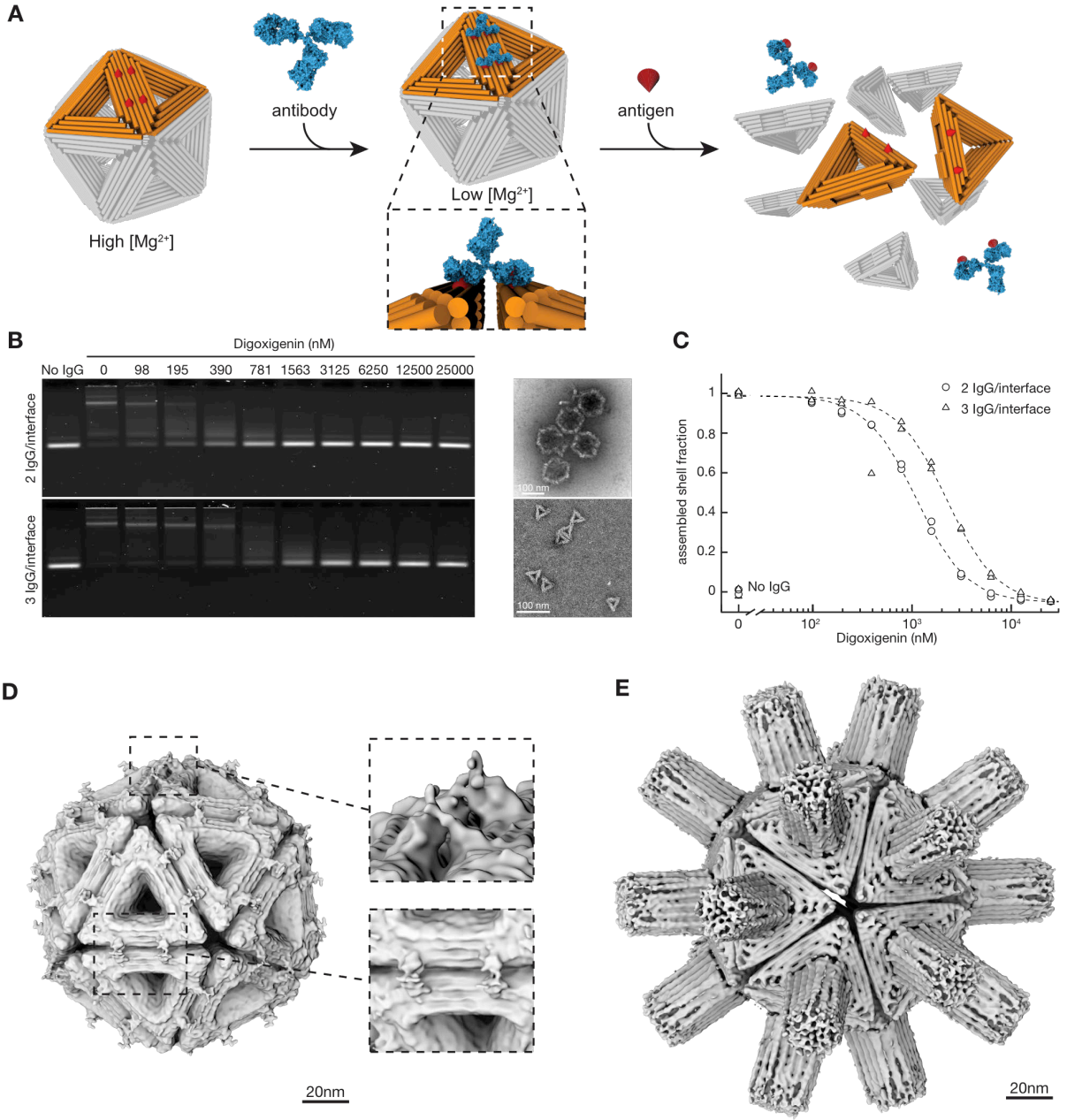

Fig. 5 | Antibody-stapled shells, antigen-sensing, surface modifications. (A) Schematics for assembling an icosahedral shell held together by antibodies in three steps: (1) high salt self-assembly of complete shells with antigens (red) conjugated at multiple sites on the edges of the triangular subunits, (2) addition of divalent IgG antibodies bridging the triangle interfaces (blue), (3) decreasing the cation^{+} concentrations. The shells are then solely stabilized by the IgG antibody staples and sensitive to the presence of soluble antigens, which can trigger disassembly. **(B)** Left: laser-scanned agarose gels on which shell samples treated with anti-digoxigenin IgG and increasing concentrations of digoxigenin were electrophoresed. Right: exemplary negative-staining TEM imagines before (top) and after addition of digoxigenin (bottom). **(C)** Dose response curves of assembled shell fraction versus concentration of added soluble antigen. Circles, triangles = two vs three antibodies bridging each triangle-triangle contact, respectively. The fraction of assembled shells was derived from the FRET efficiency between FRET pairs installed on the triangle interfaces. **(D)** Cryo-EM reconstruction of T=1 shells stabilized by antibody-antigen bridges across the subunits. Insets zoom into the electron density attributed to the antibodies, with Fc fragments pointing away from the shell. (**E**) Cryo-EM reconstruction of a T=1 shell with a central-cavity blocking DNA “spacer” module. See also Supplementary movie 8.

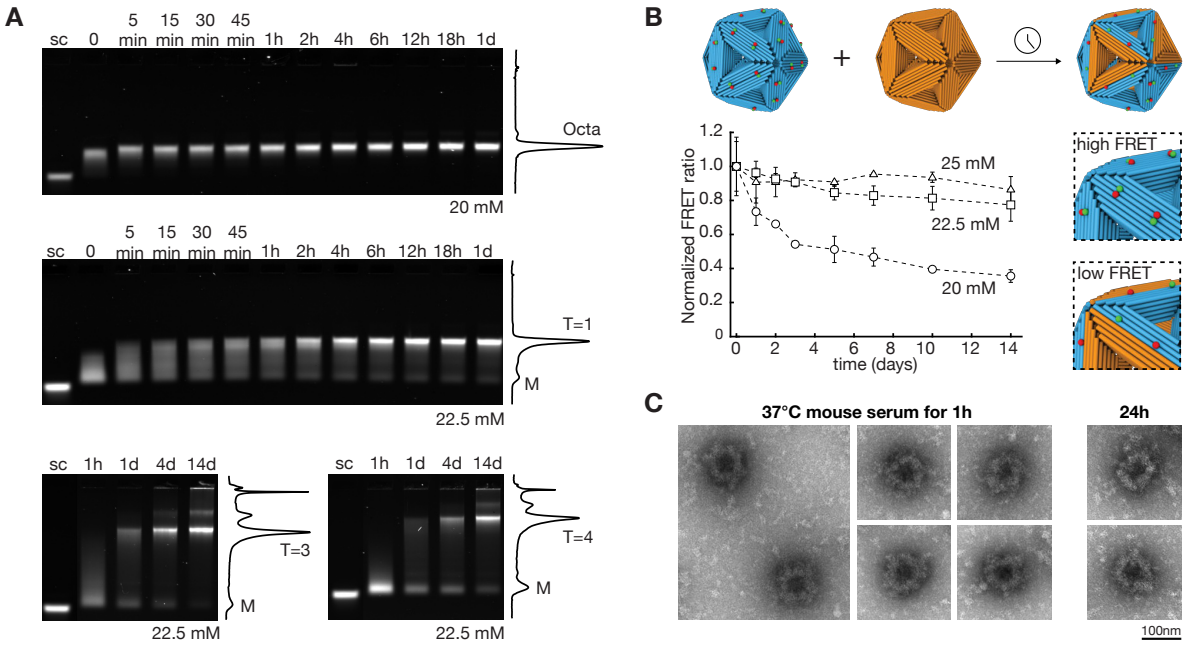

Fig. 6 | Shell yield and stability. (**A**) Laser-scanned fluorescent images of 0.5% agarose gels showing the assembly of octahedra, T=1, T=3 and T=4 shells at 40°C with a monomer concentration of 5 nM at different time points. Solid lines give cross-sectional lane intensity profiles from the 1d samples. (**B**) Triangle exchange experiments. Cyan: FRET-pair labeled T=1 shells. Orange: unlabeled shells. Symbols give FRET signals measured vs time of incubation in the presence of the indicated concentrations of Mg2+. Errors bars are SEM of duplicate measurements (design details see fig. S42B). (**C**) Negative-staining TEM image of octahedral shells coated with a 1:1 mixture of oligolysine and oligolysine-PEG and incubated for 1 h and 24h in 55% mouse serum at 37°C.

Methods

Self-assembly of shell subunits

All self-assembly experiments were performed in standardized "folding buffers" containing x mM $MgCl_2$ in addition to 5 mM Tris Base, 1 mM EDTA, 5 mM NaCl at pH 8 (FoBx). Single-scaffold-chain DNA origami objects were self-assembled in one-pot folding reactions containing 50 nM scaffold DNA and 200 nM of each staple strand. DNA origami objects containing multiple scaffolds were self-assembled using each scaffold DNA chain at 10 nm concentration and 200 nM of each staple strand. The individual scaffolds were sequence-orthogonal and designed and produced as described previously (*39, 40*). Folding buffer (FoB20) was used with x = 20 mM $MgCl_2$. All reaction mixtures were subjected to thermal annealing ramps as detailed in Table 1 in Tetrad (Bio-Rad) thermal cycling devices. Staple strands were purchased from IDT (Integrated DNA Technologies).

Object	Denaturation phase temperature (15 min) (°C)	Temperature ramp (1°C/1h)	Storage temperature (°C)	Scaffold
T_octa	65	60-56°C	20	M13 8064
T=1	65	58-54°C	20	M13 8064
T=1 -5°	65	58-54°C	20	M13 8064
T=1 +5°	65	58-54°C	20	M13 8064
T=3	65	54-52°C	20	M13 8064
T=4_iso	65	56-54°C	20	M13 8064
T=4_equi	65	58-54°C	20	M13 8064
T=9_pent	65	56-52°C	20	M13 7249
T=9_hex1	65	56-52°C	20	M13 8064
T=9_hex2	65	58-54°C	20	M13 8064
T_octa_half	65	58-54°C	20	M13 8064
T_pent T=1 (2/3 triangles)	65	58-54°C	20	M13 8064
T_ ring T=1 (2 triangles)	65	56-52°C	20	M13 8064
T_ring1 T=1 (3 triangles)	65	56-52°C	20	M13 8064
T_ring2 T=1 (3 triangles)	65	56-52°C	20	M13 8064
triangular brick	65	60-44°C	20	M13 8064

Table 1 | Temperature ramps and scaffold molecules used for self-assembly of shell building blocks. For scaffold sequences see section *Scaffold sequences* in the supplementary information. For staple sequences see design_sequnces.xlsx.

Purification of shell subunits and self-assembly of shells

All shell subunits were purified using gel purification and, if necessary, concentrated with ultrafiltration (Amicon Ultra 500 µl with 100kDa molecular weight cutoff) before self-assembling the subunits into shells. Both procedures were performed as previously described (*29*) with the following alterations: for gel purification, we used 1.5% agarose gels containing 0.5x TBE and 5.5 mM $MgCl_2$. For ultrafiltration, the same filter was filled with gel-purified sample multiple times (about 2-5 times, ~400 µl every step) in order to increase the concentration of objects that are recovered from the filter. Before putting the filter upside down in a new filter tube, we performed two washing steps with 1xFoB5 (~400 µl) to achieve well-defined buffer conditions for the shell assembly. To assemble the purified (and concentrated) shell subunits into shells we adjusted the subunit and $MgCl_2$ concentrations by adding 1xFoB5 and 1.735 M $MgCl_2$ in suitable amounts. Typical subunit concentrations were in the range of 5 nM and up to 100 nM (for cryo-EM measurements, see Table 2). Typical $MgCl_2$ concentrations for shell self-assembly were in the range of 10-40 mM. Shell

self-assembly was performed at 40°C. Reaction times were varied depending on the shell type (see Fig. 6A).

Half shells and HBV core binding

Nine staples on the inside of the triangles were modified with handles with 26 single-stranded bases at the 5' ends (seq.: 'GCAGTAGAGTAGGTAGAGATTAGGCA-oligonucleotide', for design details see figs. S39,S40). The triangles were purified and assembled as described above. Oligonucleotides complementary to the handle-sequence and modified with a thiol group at the 3' end were coupled to the HBcore 17H7 antibody using a Sulfo-SMCC (Sulfosuccinimidyl-4-[N-maleimidomethyl]cyclohexane-1-carboxylate) cross-linker. The product was subsequently purified using the *proFIRE*® from *Dynamic Biosensors*. The DNA modified antibodies were added to the assembled shells and incubated over night at 25°C. HBV core particles were incubated with the modified shells for 1-4 hours at 25°C. To assemble T=1 triangles around HBV core particles, the modified antibodies were added to single triangles. These triangles were then incubated with HBV core particles at a $MgCl_2$ concentration of 19mM for one day.

Octahedron oligolysine stabilization

The octahedral shells were assembled at 35mM $MgCl_2$ and UV cross-linked as described in (*31*) for 1h using the Asahi Spectra *Xenon Light source 300W MAX-303*. The shells were incubated in a 0.6:1 ratio with a mixture of K_{10} oligolysine and K_{10}-PEG_{5K} oligolysine (1:1) for 1h at room temperature as similarly described in (*32*). The octahedra were incubated in 55% mouse serum for 1h and 24h at 37°C. To allow imaging with negative stain the samples were diluted with PBS to a final mouse serum concentration of 5%, immediately before application to the negative stain grids.

T=1 shell exterior modification

The T=1 triangle and the triangular brick (Fig. 6C) were dimerized using single stranded DNA sticky ends protruding from the T=1 triangle. The protruding sequences contained three thymidines for flexibility plus 7 base long sequence motifs that were directly complementary to single stranded scaffold domains of the brick (fig. S41). Dimerization reactions were performed at room temperature overnight using a monomer concentration of 40 nM in the presence of 11 mM $MgCl_2$.

T=1 shell antibody stabilization and antigen-triggered disassembly

The T=1 triangles were equipped with up to three digoxigenin-modified DNA-strands per triangle side (fig. S42A) that were included in the one-pot folding reaction. Additionally, per triangle side one Cy3 and one Cy5 fluorophore were introduced, resulting in efficient Fluorescence Resonance Energy Transfer (FRET) in assembled shells, followed by a decrease in FRET efficiency upon shell disassembly. The triangles were purified and assembled as described above. 5 µL fully assembled shells in FoB25 were mixed with 2.5 µL of 80 nM IgG antibodies in FoB22.5 + 0.05% Tween-20 (Anti-Digoxigenin, Mouse monoclonal IgG1κ, clone: 1.71.256) and incubated for 2 hours at 25 °C. Subsequently, the $MgCl_2$ concentration was decreased to 12 mM by adding 40 µL FoB9 + 0.05% Tween-20 and 2.5 µL of various concentrations of Digoxigenin in FoB22.5 + 0.05% Tween-20. FRET was measured in a 384 well plate on a platereader pre-equilibrated to 30 °C (CLARIOstar, BMG labtech, λ_{ex} = 530 ± 10 nm, $\lambda_{em,A}$ = 675 ± 25 nm and $\lambda_{em,D}$ = 580 ± 15 nm). All experiments were performed in duplicates.

Cargo encapsulation in T=1 shells

Nine staples of the T=1 shell subunits were modified by adding 16 bases on the 5' ends. These nine modified staples and unmodified T=1 staples are folded with p8064 scaffold to produce T=1 triangles with nine ssDNA "handles" (fig. S31A, left). The 16-base ssDNA

handles are located on the shell-inward facing surface of the monomers. 8 of those 9 strands were oriented facing inwards towards the interior of the monomer and consequently may not have been accessible to the cargo. Single-stranded DNA cargo was prepared by attaching staple strands to the p8064 ssDNA circular scaffold with a 16 base-long overhang that was complementary to the handles on the shell subunits. An oligo containing a CY5 dye was also hybridized to the scaffold to enable fluorescence read-out by laser scanning of agarose gels (fig. S31A, middle and fig. S41C). In order to avoid having the unbound staples in cargo solution, which would passivate the monomers, 20 different staples are mixed with the scaffolds in 1:2 ratio. To anneal staples to the circular ssDNA, FOB15 buffer is used with a temperature ramp of 65°C for 15 min, 60°C to 44°C for 1h/1°C. To encapsulate gold nanoparticles, complementary handles of the monomer's handles are attached to the gold nanoparticles with a diameter of 30 nm (Cytodiagnostics, OligoREADY Gold Nanoparticle Conjugation Kit). A schematic and a negative stain TEM tomogram slice is shown in fig. S31, B and C. To increase the visibility of the encapsulated circular ssDNA in TEM images, gold nanoparticles with a diameter of 20 nm (Cytodiagnostics, OligoREADY Gold Nanoparticle Conjugation Kit) were attached to the circular ssDNA scaffold (schematic and negative stain TEM are shown in fig. S31, B and C last images from the right). T=1 shells, with & without cargo were assembled in 1xFoB20 buffer at 40°C for 3 days. Shell subunits were gel purified prior to assembly. Concentration of triangles was 16 nM. Concentration of cargo (of any type) was 0.8 nM.

Gel electrophoresis

The size distribution of folding reactions or shell assemblies was investigated using agarose gel electrophoresis. For solutions including only shell subunits, we used 1.5% agarose gels containing 0.5xTBE Buffer (22.25 mM Tris Base, 22.25 mM Boric Acid, 0.5 mM EDTA) and 5.5 mM $MgCl_2$. For solutions including oligomeric assemblies such as shells, an agarose concentration of 0.5% was used. The gel electrophoresis was performed in 0.5xTBE buffers supplemented with the same $MgCl_2$ concentration as the solutions in which the shells were incubated in. For $MgCl_2$ concentration larger than 15 mM, a surrounding ice-water bath was used for cooling the gel. The gel electrophoresis was performed for 1.5 to 2 hours at 90 V bias voltage. The agarose gels were then scanned with a Typhoon FLA 9500 laser scanner (GE Healthcare) with a pixel size of 50 µm/pix.

Negative-staining TEM

Samples were incubated on glow-discharged collodion-supported carbon-coated Cu400 TEM grids (in-house production) for 30 to 120 s depending on structure and $MgCl_2$ concentration. The grids were stained with 2% aqueous uranyl formiate solution containing 25 mM sodium hydroxide. Imaging was performed with magnifications between 10000x to 42000x. T=3 triangles were imaged on a Phillips CM100 equipped with a AMT 4Mpx CCD camera. All other negative staining data was acquired at a FEI Tecnai T12 microscope operated at 120 kV with a Tietz TEMCAM-F416 camera. TEM micrographs were high-pass filtered to remove long-range staining gradients and the contrast was auto-leveled (Adobe Photoshop CS6). To obtain detailed information on individual particles and investigate successful encapsulation negative stain EM tomography was used as a visualization technique. The grids were prepared as described above, and the tilt series acquired with magnifications between 15000x and 30000x using the FEI Tecnai 120. The stage was tilted from -50° to 50° and micrographs were acquired in 2° increments.

All tilt series were subsequently processed with IMOD (*41*) to acquire tomograms. The micrographs were aligned to each other by calculating a cross correlation of the consecutive tilt series images. The tomogram is subsequently generated using a filtered back-projection. The Gaussian-Filter used a cutoff between 0.25 and 0.5 and a fall-off of 0.035.

Cryo electron microscopy

The DNA origami concentrations used for preparing the cryo-EM grids are summarized in Table 2. Samples with concentrations higher than 100 nM were applied to glow-discharged C-flat 1.2/1.3 or 2/1 thick grids (Protochip). Samples containing shells with less than 30 nM monomer concentrations were incubated on glow-discharged grids with an ultrathin carbon film supported by a lacey carbon film on a 400-mesh copper grid (Ted Pella). The concentration of all single triangles was increased above 500 nM with PEG precipitation (*29*). 1 ml of folding reaction (~50 nM monomer concentration) was mixed with 1 ml of PEG, centrifuged at 21k rcf for 25 min and re-suspended in 50 to 100 µl 1xFoB5. The DNA-origami triangles used for assembling the shells were all gel purified and concentrated with ultrafiltration as described above before increasing the $MgCl_2$ concentration. Plunge freezing in liquid ethane was performed with a FEI Vitrobot Mark V with a blot time of 1.5 to 2 s, a blot force of -1 and a drain time of 0 s at 22°C and 95% humidity. The samples with less than 100 nM monomer concentrations were incubated on the support layer for 60 to 90 s before blotting. All cryo-EM images were acquired with a Cs-corrected Titan Krios G2 electron microscope (Thermo Fisher) operated at 300 kV and equipped with a Falcon III 4k direct electron detector (Thermo Fisher). We used the EPU software for automated single particle acquisition. See Table 2 for microscope settings for all individual datasets. The defocus for all acquisitions was set to -2 µm. The image processing was done at first in RELION-2 (*42*) and then later in RELION-3 (*43*). The recorded movies were subjected to MotionCor2 (*44*) for movie alignment and CTFFIND4.1 (*45*) for CTF estimation. After reference-free 2D classification the best 2D class averages, as judged by visual inspection, were selected for further processing. A subset of these particles was used to calculate an initial model. After one to two rounds of 3D classification, the classes showing the most features or completely assembled shells were selected for 3D auto-refinement and post-processing. For the corresponding shells octahedral (O) or icosahedral (I1) symmetry was used for the last two steps.

Object	Concentration (nM)	# of particles	# of fractions	Dose (e/A^2)	Pixel size (A/pix)	Resolution of resulting 3D map (A)	Symmetry
Octa monomer	700	16524	5	42.57	2.28	18.69	C1
T=1 monomer	500	9496	7	51.16	2.28	20.27	C1
T=3 monomer	500	11080	7	53.17	2.28	19.09	C1
T=4_iso	500	16904	7	48.53	2.28	17.22	C1
T=4_equi	500	34288	7	48.26	2.28	21.21	C1
T=9_pent	800	25053	8	47.9	1.79	14.92	C1
T=9_hex1	800	38498	13	36.85	1.79	12.92	C1
T=9_hex2	800	11481	8	48	1.79	15.04	C1
Octa shell (17.5mM)	130	3384	11	42.71	2.28	19.64	O
T=1 shell (20 mM)	110	2578	10	51.11	2.28	21	I1
T=1 shell (25 mM)	50 (lacey carbon grid)	720	7	31.26	2.28	22.21	I1
T=3 shell (20 mM)	20	612	-	22.96	3.71	36.15	I1
T=4 shell (25 mM)	21 (T_iso) 7 (T_equi)	255	-	25	3.71	47.87	I1
Octa_half Shell (30mM)	180	6801	10	40.44	2.9	20.41	C4
Octa_half shell (30mM) + HBV core	40	2707	7	44.38	2.9	23	C1
T=1_half	180	8725	10	40.44	2.9	15.16	C1

shell (2 triangles, 30mM)							
T=1_half shell + HBV core (2 triangles, 30mM)	50	1770	7	44.79	2.9	23	C5
T=1_15mer shell (3 triangles, 30mM)	210	3194	10	29.17	2.9	22.3	C5
spiky shell (22.5mM)	150	3847	8 (dataset1) 11 (dataset 2)	25.76 (dataset1) 30.00 (dataset 2)	3.76	22	I1
T=1 shell + Digox. + 2 AB	100	629	18	42.44	2.9	22.66	I1
triangular brick	1000	38132	7	78.6	2.28	11.9	C1

Table 2 | Cryo-EM imaging conditions.

In vitro virus blocking ELISA

Various concentrations of assembled half-T1 shells were incubated overnight at room temperature with 2 nM oligonucleotide-conjugated capture antibody (anti-HBc 17H7, Isotype IgG-2b) in FoB30-T (FoB30 + 0.05% Tween-20). The next day the pre-incubated mixtures were added to 5 pM HBV core particles and incubated overnight at room temperature, yielding 1 nM capture antibody, 2.5 pM HBV core particle and 0-200 pM half-T=1 shells. A flat-bottom transparent 96 well microplate (Nunc MaxiSorp) was treated overnight at 4 °C with 100 µl/well anti-CAgHB antibody (1 µg/ml in PBS). After washing 4 times with 200 µl/well PBS-T (PBS + 0.05% Tween-20) the well surface was blocked by incubating with 200 µl/well 5% bovine serum albumin in PBS for 2 hours at room temperature. After washing 4 times with 200 µl/well FoB30-T, 90 µl of the pre-incubated samples were added to the wells and incubated for 2 hours at room temperature, followed by washing and subsequent incubation for 1 hour with 100 µl/well horseradish peroxidase conjugated detection antibody (anti-CAgHB-HRP in FoB30-T). After washing with FoB30-T, 100 µl/well HRP substrate (3,3',5,5'-Tetramethylbenzidine, lifetechnologies) was added and product formation was monitored in time by measuring the absorbance at 650 nm with a 60 s interval in a platereader pre-equilibrated to 30 °C (CLARIOstar, BMG labtech). HRP activity was calculated by fitting linear regression slopes to the linear regime of the kinetic data (typically the first 5 minutes). Virus blocking efficiency was calculated relative to a control of HBV core particles only and blank measurements. All experiments were performed in triplicates. Antibodies used for the ELISA were kindly provided by Centro De Ingenieria Genetica y Biotecnologia de sancti spiritus in Cuba.

Helium Ion Microscopy (HIM)

Imaging was performed with negative-stained TEM grids coated with a 5 nm layer of AuPd using a Quorum Q150T sputter coater in ORION Nanofab (Zeiss). We used an acceleration voltage of 30 kV and a beam current of 0.3 to 0.4 pA. The images were acquired in scanning mode with an Everhart-Thornley 2k detector.

Production of HBV core particles

Hepatitis B virus core particles of genotype D (subtype ayw2) were produced recombinantly in *E. coli* K802 and BL21 cells (purchased from purchased from the Latvian Biomedical Research and Study Centre, Riga, Latvia). Briefly, particles were obtained by sonication and

clarification from bacterial protein extracts and purified by ammonium sulphate precipitation and subsequent anion exchange and size exclusion chromatography as described (*46*). Final preparations were constantly kept at 4 °C in the dark in conventional PBS (including 0.05% NaN_3, 1 mM DTT).

Production of Anti-HBc antibody

Anti-HBV core (anti-HBc) antibody 17H7 (Isotype IgG-2b) was produced by the Monoclonal Antibody Core Facility at Helmholtz Zentrum München in Munich (HMGU). Briefly, mouse HBc-recognizing B cells were generated by common hybridoma technology. The mice were challenged with the peptide NLEDPASRDLVVC (aa 75-86 of HBV core). Mouse hybridoma clones were selected and secreted antibodies were analyzed by immune staining and precipitation of HBcAg and ELISA for native antigen recognition and by Western Blot analysis for detection of denatured antigen. Final 17H7 preparations were purified via standard affinity chromatography using a protein A/G column and concentrated to 0.8 mg/mL (5.33 µM) of protein and kept in conventional PBS (137 mM NaCl, 10 mM Phosphate, 2.7 mM KCl, pH 7.4) at 4 °C in the dark.

REFERENCES

1. C. Gortazar *et al.*, Crossing the interspecies barrier: opening the door to zoonotic pathogens. *PLoS pathogens* **10**, e1004129 (2014).
2. S. S. Morse *et al.*, Prediction and prevention of the next pandemic zoonosis. *Lancet* **380**, 1956-1965 (2012).
3. B. K. Ganser-Pornillos, O. Pornillos, Restriction of HIV-1 and other retroviruses by TRIM5. *Nat Rev Microbiol* **17**, 546-556 (2019).
4. K. A. Skorupka *et al.*, Hierarchical assembly governs TRIM5alpha recognition of HIV-1 and retroviral capsids. *Sci Adv* **5**, eaaw3631 (2019).
5. M. Legendre *et al.*, Thirty-thousand-year-old distant relative of giant icosahedral DNA viruses with a pandoravirus morphology. *Proceedings of the National Academy of Sciences of the United States of America* **111**, 4274-4279 (2014).
6. F. H. Crick, J. D. Watson, Structure of small viruses. *Nature* **177**, 473-475 (1956).
7. J. B. Bale *et al.*, Accurate design of megadalton-scale two-component icosahedral protein complexes. *Science* **353**, 389-394 (2016).
8. N. P. King *et al.*, Accurate design of co-assembling multi-component protein nanomaterials. *Nature* **510**, 103-108 (2014).
9. Y. T. Lai *et al.*, Structure of a designed protein cage that self-assembles into a highly porous cube. *Nature chemistry* **6**, 1065-1071 (2014).
10. G. L. Butterfield *et al.*, Evolution of a designed protein assembly encapsulating its own RNA genome. *Nature* **552**, 415-420 (2017).
11. P. W. K. Rothemund, Folding DNA to create nanoscale shapes and patterns. *Nature* **440**, 297-302 (2006).
12. S. M. Douglas *et al.*, Self-assembly of DNA into nanoscale three-dimensional shapes. *Nature* **459**, 414-418 (2009).
13. C. E. Castro *et al.*, A primer to scaffolded DNA origami. *Nature methods* **8**, 221-229 (2011).
14. R. Veneziano *et al.*, Designer nanoscale DNA assemblies programmed from the top down. *Science* **352**, 1534 (2016).
15. E. Benson *et al.*, DNA rendering of polyhedral meshes at the nanoscale. *Nature* **523**, 441-444 (2015).
16. K. E. Dunn *et al.*, Guiding the folding pathway of DNA origami. *Nature* **525**, 82-86 (2015).
17. X. C. Bai, T. G. Martin, S. H. Scheres, H. Dietz, Cryo-EM structure of a 3D DNA-origami object. *Proceedings of the National Academy of Sciences of the United States of America* **109**, 20012-20017 (2012).
18. J. J. Funke, H. Dietz, Placing molecules with Bohr radius resolution using DNA origami. *Nature nanotechnology* **11**, 47-52 (2016).
19. R. Iinuma *et al.*, Polyhedra self-assembled from DNA tripods and characterized with 3D DNA-PAINT. *Science* **344**, 65-69 (2014).
20. R. Jungmann *et al.*, DNA origami-based nanoribbons: assembly, length distribution, and twist. *Nanotechnology* **22**, 275301 (2011).
21. W. Liu, H. Zhong, R. Wang, N. C. Seeman, Crystalline two-dimensional DNA-origami arrays. *Angew Chem Int Ed Engl* **50**, 264-267 (2011).
22. Y. Suzuki, M. Endo, H. Sugiyama, Lipid-bilayer-assisted two-dimensional self-assembly of DNA origami nanostructures. *Nat Commun* **6**, 8052 (2015).
23. Y. Ke *et al.*, DNA brick crystals with prescribed depths. *Nature chemistry* **6**, 994-1002 (2014).
24. K. F. Wagenbauer, C. Sigl, H. Dietz, Gigadalton-scale shape-programmable DNA assemblies. *Nature* **552**, 78-83 (2017).
25. D. L. Caspar, A. Klug, Physical principles in the construction of regular viruses. *Cold Spring Harbor symposia on quantitative biology* **27**, 1-24 (1962).

26. R. Twarock, A. Luque, Structural puzzles in virology solved with an overarching icosahedral design principle. *Nat Commun* **10**, 4414 (2019).
27. S. M. Douglas *et al.*, Rapid prototyping of 3D DNA-origami shapes with caDNAno. *Nucleic acids research* **37**, 5001-5006 (2009).
28. C. Maffeo, J. Yoo, A. Aksimentiev, De novo reconstruction of DNA origami structures through atomistic molecular dynamics simulation. *Nucleic acids research* **44**, 3013-3019 (2016).
29. K. F. Wagenbauer *et al.*, How we make DNA origami. *Chembiochem : a European journal of chemical biology*, (2017).
30. M. Langecker *et al.*, Synthetic lipid membrane channels formed by designed DNA nanostructures. *Science* **338**, 932-936 (2012).
31. T. Gerling, M. Kube, B. Kick, H. Dietz, Sequence-programmable covalent bonding of designed DNA assemblies. *Sci Adv* **4**, eaau1157 (2018).
32. N. Ponnuswamy *et al.*, Oligolysine-based coating protects DNA nanostructures from low-salt denaturation and nuclease degradation. *Nat Commun* **8**, 15654 (2017).
33. F. Praetorius, H. Dietz, Self-assembly of genetically encoded DNA-protein hybrid nanoscale shapes. *Science* **355**, (2017).
34. G. Zhang, Pomplun, S., Loftis, A.R., Loas, A., Pentelute, B.L., The first-in-class peptide binder to the SARS-CoV-2 spike protein. *bioRxiv*, (2020).
35. U. Ohto *et al.*, Structural basis of CpG and inhibitory DNA recognition by Toll-like receptor 9. *Nature* **520**, 702-705 (2015).
36. L. Andreeva *et al.*, cGAS senses long and HMGB/TFAM-bound U-turn DNA by forming protein-DNA ladders. *Nature* **549**, 394-398 (2017).
37. M. F. Naso, B. Tomkowicz, W. L. Perry, 3rd, W. R. Strohl, Adeno-Associated Virus (AAV) as a Vector for Gene Therapy. *BioDrugs* **31**, 317-334 (2017).
38. D. Wang, P. W. L. Tai, G. Gao, Adeno-associated virus vector as a platform for gene therapy delivery. *Nat Rev Drug Discov* **18**, 358-378 (2019).
39. F. A. S. Engelhardt *et al.*, Custom-Size, Functional, and Durable DNA Origami with Design-Specific Scaffolds. *ACS nano*, (2019).
40. B. Kick, F. Praetorius, H. Dietz, D. Weuster-Botz, Efficient Production of Single-Stranded Phage DNA as Scaffolds for DNA Origami. *Nano letters*, (2015).
41. J. R. Kremer, D. N. Mastronarde, J. R. McIntosh, Computer visualization of three-dimensional image data using IMOD. *Journal of structural biology* **116**, 71-76 (1996).
42. D. Kimanius, B. O. Forsberg, S. H. Scheres, E. Lindahl, Accelerated cryo-EM structure determination with parallelisation using GPUs in RELION-2. *Elife* **5**, (2016).
43. J. Zivanov *et al.*, New tools for automated high-resolution cryo-EM structure determination in RELION-3. *Elife* **7**, (2018).
44. S. Q. Zheng *et al.*, MotionCor2: anisotropic correction of beam-induced motion for improved cryo-electron microscopy. *Nature methods* **14**, 331-332 (2017).
45. A. Rohou, N. Grigorieff, CTFFIND4: Fast and accurate defocus estimation from electron micrographs. *Journal of structural biology* **192**, 216-221 (2015).
46. I. Sominskaya *et al.*, A VLP library of C-terminally truncated Hepatitis B core proteins: correlation of RNA encapsidation with a Th1/Th2 switch in the immune responses of mice. *PloS one* **8**, e75938 (2013).